

1 Harvest wind energy from a vibro-impact DEG embedded into a bluff body

2 Z. H. Lai^a, J. L. Wang^{b,*}, C. L. Zhang^c, G. Q. Zhang^a, D. Yurchenko^d,

3 ^a Guangdong Provincial Key Laboratory of Micro/Nano Optomechanics Engineering, College of
4 Mechatronics and Control Engineering, Shenzhen University, Shenzhen 518060, P. R. China

5 ^b Engineering Research Center of Energy Saving Technology and Equipment of Thermal Energy
6 System, Ministry of Education, Zhengzhou University, Zhengzhou 450000, P. R. China

7 ^c School of Mechatronics Engineering, Nanchang University, Nanchang 330031, P. R. China

8 ^d Institute of Mechanical, Process & Energy Engineering, Heriot-Watt University, Edinburgh EH14
9 4AS, UK

10
11 **Abstract:** A novel wind energy harvester is proposed and studied in this paper. The system
12 contains a vibro-impact (VI) dielectric elastomer generator (DEG) that can convert vibrational
13 energy into electrical one through the impacts of a rigid ball inside. The VI DEG is embedded
14 into a cuboid bluff body connecting to a galloping-based system. Thus, wind energy is
15 converted to the vibrations of the bluff body, which are further harvested by the DEG. The
16 dynamic and electrical behaviors of the proposed system under wind environments are
17 analyzed theoretically, whereas some key parameters of the system are identified
18 experimentally, including a wind tunnel test for the bluff body and material tests for the
19 dielectric elastomer membrane. The dynamic and electrical outputs of the system under
20 different wind speeds are studied through numerical simulations. The influences of the wind
21 speed and some system parameters on the system energy harvesting (EH) performance are
22 further discussed. Thus, the priority of the proposed system in wind EH is presented and some
23 effective solutions to design the system and improve the system EH performance are
24 proposed.

25
26 **Keywords:** wind energy; dielectric elastomer generator; vibration; galloping; vibro-impact

27 28 1. Introduction

29 Energy crises and environmental issues have become worldwide problems. One of the most
30 important solutions to solve these problems is exploring and utilizing green sustainable
31 energies from solar, nuclear sources and ambient vibrations, which can not only be easily
32 found in a variety of machines, human motions, building and other civil structures [1], but
33 also be achieved from wind or water induced vibrations [2-4].

34 Wind energy harvesting devices [5], which utilize different mechanical structures to
35 convert ubiquitous wind energy into electricity, have attracted much attention in the past
36 decade. These devices cover various scales from large-scale devices including wind turbines
37 to small- and micro-scale wind energy harvesters, which are suitable for many applications
38 such as wireless sensors [6,7], automotive [8] and other sectors [9,10].

39 Up to now the majority of investigations on small-scale wind energy harvesters have been
40 focused on the use of piezoelectricity (PE) materials [11-16]. Comparing to other competitive

* Corresponding author at:

Engineering Research Center of Energy Saving Technology and Equipment of Thermal Energy System,
Ministry of Education, Zhengzhou University, Zhengzhou 450000, P. R. China,
Email address: jlwang@zzu.edu.cn (J. L. Wang)

1 vibration energy harvesting (VEH) devices including electromagnetic (EM) [17,18],
2 electrostatic (ES) [19] and triboelectric (TE) [20] devices, the PE VEH devices have simple
3 structures and relatively high energy conversion efficiencies. Currently, PE prototypes have
4 been established to harvest wind-induced vibrational energy including vortex [21], galloping
5 [22,23], flutter [24], and wake galloping [25] –induced vibrations. However, these devices are
6 less versatile than desired [26] and have certain limitations and shortcomings, one of which is
7 their ability to generate only a relatively small amount of energy. These factors restrict the
8 areas of application of PE-based wind energy harvester.

9 In recent years, dielectric elastomer (DE) materials have shown their potential in VEH due
10 to their high energy density, large deformability, good electromechanical conversion
11 efficiency and moderate or low cost, etc. [27,28]. The first DE-based energy harvester was
12 proposed by Pelerine et al back in 2001 [29]. After that, a type of novel ES VEH devices
13 where the DE membranes (DEMs) are used as changeable capacitors instead of the parallel
14 plates [30] has been proposed. This type of energy harvesters, which are also called dielectric
15 elastomer generators (DEGs), can convert linear, nonlinear or rotational motions within a
16 wide frequency range [31] with a relative high energy density (up to 0.4 J/g), which is at least
17 an order of magnitude higher than that of EM, ES and PE energy harvesters [32], especially at
18 low-frequency operating conditions. Moreover, the highest power density that has been
19 achieved in a DEG experimentally is $3.8 \mu\text{W}/\text{mm}^3$, which is higher than those in EM (2.21
20 $\mu\text{W}/\text{mm}^3$), ES ($2.16 \mu\text{W}/\text{mm}^3$), and PE ($0.375 \mu\text{W}/\text{mm}^3$) [33,34].

21 In order to fully take advantage of the DE materials in VEH, Suo et al [35] established the
22 DE theory based on thermodynamics and continuum mechanics. The basic material properties
23 of the DEM and failure mechanisms, including material rupture, loss of tension, electrical
24 breakdown, and electromechanical instability, were established [32,36-39]. A detailed model
25 that describes the four cycling phases of DE-based EH was developed in [40]. A new
26 electrical scheme has been designed and was first set out by Shian et al [41]. This scheme,
27 which is also called the “triangular” scheme, claimed to have the highest energy density.
28 These research results have laid the foundation for further investigations in DEGs. Up to now,
29 several DEGs have been developed such as the ocean wave generator [42,43], human motions
30 energy harvester [44], etc.

31 Although many achievements have been made in the DEG research, most of the proposed
32 DEGs focus on the stretching and relaxation of DEMs at the material level, which meaning
33 that they are not suitable to work in real vibrational environments. Currently, a vibro-impact
34 (VI) DEG system has been proposed by the authors previously [45-47]. The research results
35 have shown that the proposed DEG, which is based on the out-of-plane deformations of the
36 DEMs under the impacts of a rigid ball, is expected to work in practical vibrational
37 environments and achieve high electrical power.

38 In this paper, the proposed VI DEG is further improved to harvest wind energy, thus
39 expanding the working environment of DEGs and the harvesting approaches for wind energy.
40 Inspired by a galloping-based system, which has been proved the most effective and feasible
41 form in energy scavenging from flow-induced vibrations [48], we propose a novel
42 galloping-based wind energy harvester that contains the VI DEG embedded into a cuboid
43 bluff body under the streamlined wind environment. In Section 2, the wind energy harvester is
44 introduced and the dynamic and electrical behaviors of the system are analyzed. Experimental

1 schemes and results are presented to identify some key parameters in Section 3. In Section 4,
 2 the dynamic and electrical outputs of the proposed system under different wind speeds are
 3 studied through numerical simulations. In Section 5, the influences of the wind speeds and
 4 some system parameters on the system EH performance are discussed. Conclusions are drawn
 5 in Section 6.

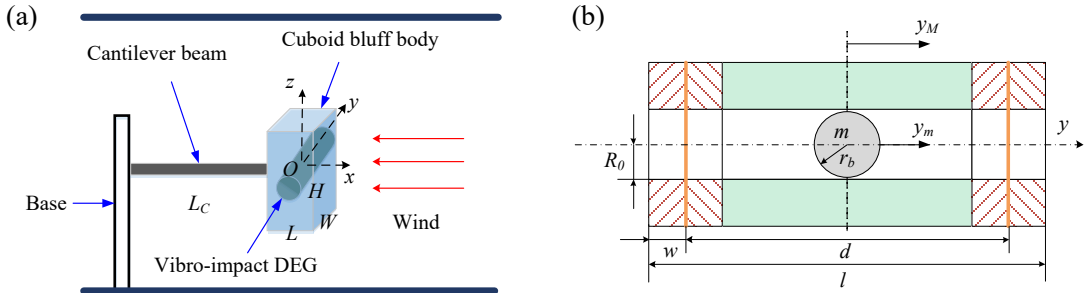
6 2. Theoretical analysis

7 2.1 Introduction of the wind energy harvester

8 A wind energy harvester, which comprises a galloping-based system consisting of a cuboid
 9 bluff body, a cantilever beam and a VI DEG embedded horizontally into the bluff body, is
 10 proposed in this paper as shown in Figure 1(a).

11 It can be seen from Figure 1(a) that a cuboid bluff body, whose length, height and width are
 12 L , H and W , respectively, is attached to the free end of a cantilever beam with length L_C
 13 connecting to a rigid base. It is assumed that the wind passes over the face of the bluff body
 14 perpendicularly. For the convenience of further analysis, a Cartesian $xyz-O$ coordinate
 15 system is introduced as follows: the coordinate origin locates at the center point of the cuboid
 16 bluff body; x -axis indicates the orientation parallel to the incoming wind flow pointing
 17 towards the bluff body's front face; y -axis indicates the horizontal direction perpendicular to
 18 the x -axis; z -axis indicates the vertical orientation.

19 A VI DEG [46], which is shown in Figure 1(b), is embedded into the cuboid bluff body.
 20 The DEG comprises a hollow cylinder with inner radius R_0 , an inner ball of mass m and
 21 radius r_b rolling/sliding freely inside the cylinder and two pre-stretched circular DEMs at
 22 both ends of the cylinder. The effective radius of the membranes equals to R_0 . Both
 23 pre-stretched membranes are sandwiched between two compliant electrodes and wires are
 24 connected to both sides of each membrane. Each membrane is fixed between two identical
 25 cylindrical frames with a width w and then connected to the cylinder, thus simplifying the
 26 assembly of the DEG. The length of the DEG is denoted as l ($l \leq W$). Thus, the distance
 27 between two membranes can be written as $d = l - 2w$. As shown in Figure 1(b), a y
 28 -direction is defined as the rightward orientation of the DEG along its axis, and the origin of
 29 the coordinate system for the inner ball coincides with that of the cylinder and is set in the
 30 center of the cylinder. The friction between the ball and the slot is quite small and therefore it
 31 is ignored.



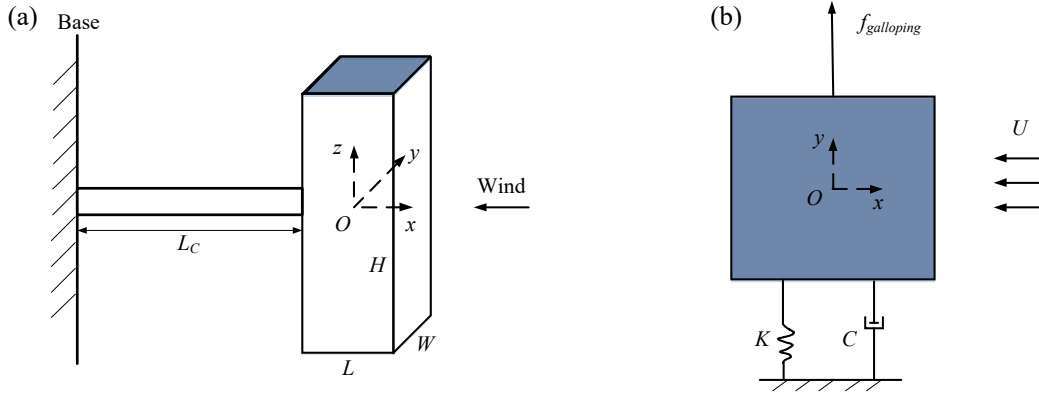
32 Figure 1 (a) System structure and (b) the scheme of the VI DEG.

34 The proposed wind energy harvester can work as follows. The system can arouse galloping

1 when the wind passes over the bluff body due to the aerodynamic-instability induced by the
 2 wind. Negative aerodynamic damping caused by galloping can keep the vibratory system in a
 3 quite strong oscillatory state. Thus, the bluff body can vibrate approximately following the
 4 y -direction as well as the outer structure of the DEG (the cylinder and the four frames with
 5 the DEMs fixed). If the motion amplitude of the outer structure is large enough, either
 6 membrane will impact the inner ball and engage its motion. The ball then will impact both
 7 membranes intermittently and electrical energy can be harvested by using the
 8 mechanical-electrical energy conversion properties of the DE materials.

9 2.2 Vibration analysis of the bluff body

10 The schematic diagram of the proposed energy harvester under wind is presented in Figure
 11 2(a) and the dynamics model is presented shown in Figure 2(b).



12 Figure 2 (a) The schematic diagram of the proposed energy harvester under wind and (b) the
 13 dynamics model (top view).
 14

15 The motion of the cuboid bluff body, which is located at the free end of the cantilever beam
 16 and is suffered from the continuous wind, is governed by the following equation:

$$17 \quad M \frac{d^2 y_M(t)}{dt^2} + C \frac{dy_M(t)}{dt} + K y_M(t) = f_{galloping} \quad (1)$$

18 In Eq. (1), M is the effective mass of the vibratory system, which is contributed by the
 19 masses of the bluff body, the cantilever beam mass and mass of the outer structure of the DEG;
 20 C is the effective damping defined as $C = 2\zeta M \omega_{nsc}$, where ζ and ω_{nsc} are the
 21 mechanical damping ratio and the natural frequency of the system, respectively; K is the
 22 stiffness of the system decided by $K = M \omega_{nsc}^2$; $f_{galloping}$ is the aerodynamic forces acting on
 23 the bluff body. Thus, $y_M(t)$, which is the solution of Eq. (1), indicates the transverse
 24 displacement of the bluff body, where $f_{galloping}$ can be further calculated as:

$$25 \quad f_{galloping} = 0.5 \rho W H U^2 \left[A_1 \left(\frac{\dot{y}_M(t)}{U} + y^* \right) + A_3 \left(\frac{\dot{y}_M(t)}{U} + y^* \right)^3 \right] \quad (2)$$

26 Here, U denotes the wind speed; ρ is the air density; $y^* = \beta y_M(t)$ is the rotation angle
 27 of the bluff body with $\beta = 11.67$ [49], where β - the coefficient between the transverse
 28 displacement and the rotation angle of the bluff body; A_1 and A_3 are the aerodynamic
 29 coefficients that should be identified experimentally, but these values are mainly depended on
 30 the shape of the bluff body. Thus, by combing Eqs. (1) and (2), the vibration output $y_M(t)$

1 of the bluff body under wind with a given speed can be obtained by solving these nonlinear
2 equations.

3 2.3 Energy harvesting from the VI DEG

4 The vibrational output of the cuboid bluff body, on another side, can be regarded as the
5 excitation of the VI DEG. Thus, the dynamic behavior of the DEG system can be obtained
6 and its energy harvesting process can be further analyzed.

7 Considering that the DEG is set up horizontally, and the friction between the inner ball and
8 the cylinder is ignored, the inner ball experiences no outer force between impacts. Therefore,
9 the ball's velocity will not be changed until it impacts one of the membranes. By defining the
10 ball's displacement as $y_m(t)$, we introduce the relative displacement $\Delta y = y_m - y_M$ as the
11 difference of displacements between the ball and the cylinder, and $s = l - 2w - 2r_b$ as the
12 largest distance the ball can travel between two membranes. Thus, it is easy to understand that
13 impacts occur under the following conditions:

$$14 \begin{cases} \Delta y = y_m - y_M = -s/2, y'_m < y'_M & \text{when the ball impacts the left membrane} \\ \Delta y = y_m - y_M = s/2, y'_m > y'_M & \text{when the ball impacts the right membrane} \end{cases} \quad (3)$$

15 At each impact, the velocities of the ball and the cylinder are governed by:

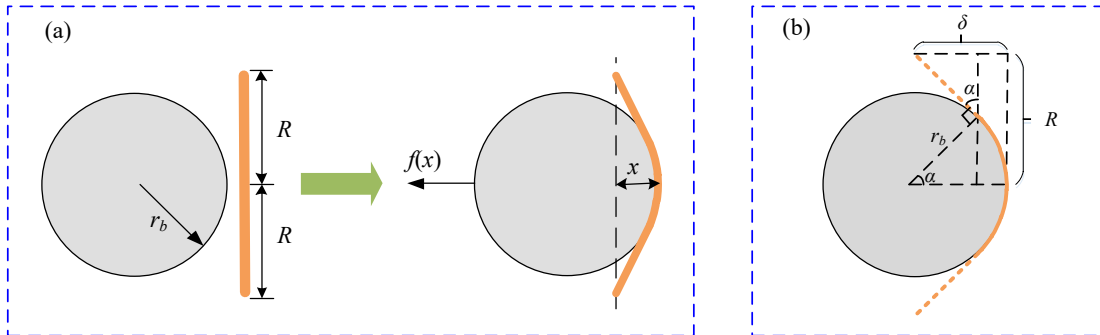
$$16 \frac{v_{m+} - v_{M+}}{v_{m-} - v_{M-}} = r \quad (4)$$

17 where r ($0 < r < 1$) is the coefficient of restitution (COR) of the membrane under the ball's
18 impacts; v_{m-} and v_{m+} represent the velocities of the ball just before and after each impact,
19 and v_{M-} and v_{M+} those of the cylinder. Considering that the mass of the ball is relatively
20 small compared to that of the rest of the system, the cylinder's velocity can be regarded as
21 unaffected by impacts, i.e., $v_M = v_{M-} = v_{M+}$. Thus, Eq. (4) can be simplified as:

$$22 v_{m+} = -rv_{m-} + (r+1)v_M \quad (5)$$

23 It can be seen from the previous analyses that if the value of r is given, the ball's motion
24 under the cylinder's movement can be calculated. The values of r will be identified through
25 experiments in next section.

26 At each impact, the membrane is deformed by the ball, as shown in Figure 3(a), where x
27 defines the deflection direction of the membrane's center. At the membrane's deformation
28 shown in Figure 3(b) and indicated by δ , the membrane's dimensions of its largest area A'
29 and smallest thickness h' can be calculated from the geometrical consideration [46]. The
30 total membrane are in 3D space is:



31
32 Figure 3 (a) The change of the membrane's shape under the ball's impact and (b) the membrane's
33 dimensions at its largest deformation.

1
$$A' = A'_1 + A'_2 \quad (6)$$

2 where A'_1 and A'_2 represent the spherical cap (shown as the dashed line) and conical
3 fulcrum (shown as the solid line) respectively for the membrane:

4
$$\begin{cases} A'_1 = 2\pi r_b (r_b - r_b \cos \alpha) = 2\pi r_b^2 (1 - \cos \alpha) \\ A'_2 = \frac{\pi R_0^2 - \pi (r \sin \alpha)^2}{\cos \alpha} \end{cases} \quad (7)$$

5 The value of α is determined by the largest deflection δ and the dimensional parameters:

6
$$\cos \alpha = \frac{-2r_b (\delta - r_b) + 2R_0 \sqrt{R_0^2 + \delta^2 - 2\delta r_b}}{2[R_0^2 + (\delta - r_b)^2]} \quad (8)$$

7 Due to the membrane's incompressibility (its volume remain the same), its thickness at
8 largest deformation can be obtained:

9
$$h' = \frac{\pi R^2 h_0}{A'} \quad (9)$$

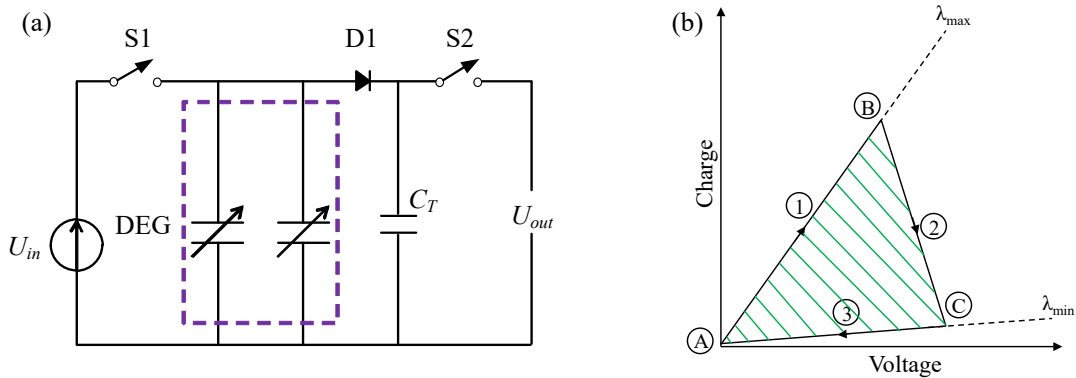
10 The values of this parameter at impacts will be studied through experiments in next
11 section as well.

12 According to the dimensions of the membrane, the minimum capacitance of the membrane
13 at its original shape and the maximal one at its largest deformation at one impact can be
14 obtained as:

15
$$C_0 = C_{\min} = \frac{\epsilon_0 \epsilon_r A_0}{h_0} = \frac{\epsilon_0 \epsilon_r Vol}{h_0^2} \quad (10)$$

16
$$C' = C_{\max} = \frac{\epsilon_0 \epsilon_r A'}{h'} = \frac{\epsilon_0 \epsilon_r Vol}{h'^2} \quad (11)$$

17 where $\epsilon_0 = 8.854 \times 10^{-12}$ F/m is the vacuum permittivity, Vol the constant volume of the
18 DE material, and ϵ_r the relative permittivity of the DE material, which will be studied
19 through theoretical analysis and experimental verification in next section. By connecting the
20 membranes to the energy harvesting circuit shown in Figure 4, the system electrical output can
21 be further calculated. This energy harvesting circuit (see Figure 4(a)), which was first set out
22 by Shian [41], is claimed to be able to produce the highest electricity gain trough a so-called
23 "triangular" scheme shown in Figure 4(b). Using this energy harvesting circuit, the output
24 voltage at each impact can be calculated as:



25
26 Figure 4 (a)Energy harvesting circuit used to control the electromechanical cycle showing a

1 power supply providing input voltage, the DEG, a transfer capacitor (C_T), a diode (D1), a
 2 charging switch (S1), harvesting switch (S2); (b) The electromechanical harvesting scheme is
 3 shown by the triangle A-B-C-A on the charge-voltage work-conjugate plane.

$$4 \quad V_{out} = V_C = \frac{C_{max} + C_T}{C_{min} + C_T} V_{in} \quad (12)$$

5 where C_T is the capacitance of the transfer capacitor. It was reported that most electrical
 6 energy can be harvested through this circuit when $C_T = 1.2C_0$. Further, the electrical energy
 7 gain at each impact can be obtained by calculating the area of the shaded green section shown
 8 in Figure 4(b) [50]:

$$9 \quad E = \frac{1}{2} V_{in} V_{out} (C_{max} - C_{min}) \quad (13)$$

10 Moreover, when a steady-state vibrations are considered, i.e., impacts occur during a long
 11 time, the total energy harvested from the DEG and the generated power can be calculated as:

$$12 \quad E_{total} = \sum_{i=1}^n E_i \quad (14)$$

$$13 \quad P = \frac{E_{total}}{t_2 - t_1} \quad (15)$$

14 where t_1 and t_2 are the start time and end time for calculation, respectively; E_i is the
 15 harvested energy at i^{th} impact and n is the number of impacts during the time interval.

16 3. Experiments

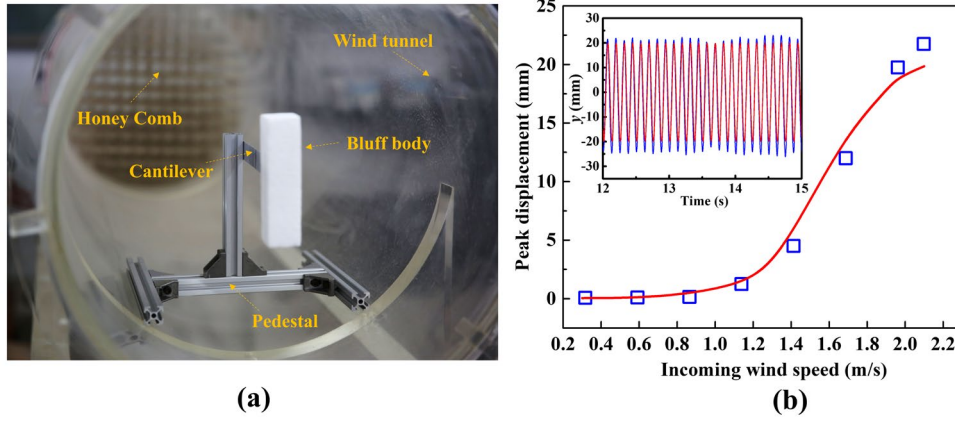
17 According to the theoretical analyses in Section 2, it is noted that some parameters should
 18 be further identified through experiments for further numerical simulations. The experiments
 19 and results are presented in this section.

20 3.1 Identification of aerodynamic coefficients A_1 and A_3

21 According to [49], the values of the empirical aerodynamic coefficients can be selected as
 22 $A_1 = 2.3$ and $A_3 = -18$, respectively. To identify these values, a galloping prototype was
 23 fabricated and tested in a wind tunnel, as shown in Figure 5(a). The prototype is built of a
 24 cuboid bluff body and a pure aluminum cantilever beam, and the bluff body is attached to the
 25 free end of the cantilever beam. The effective mass of the vibratory system is $M = 5.2515$ g,
 26 and the dimensional parameters are $L_C = 200$ mm, $L = W = 32$ mm and $H = 118$ mm,
 27 respectively. During the wind tunnel test, a wind tunnel with a diameter of 400 mm was used
 28 to produce an incoming wind for the prototype, and a flow stabilizing device with honeycomb
 29 structure was installed at the inlet of the wind tunnel to reduce the flow disturbance. The wind
 30 speed and the vibration amplitude of the bluff body were measured by a hot-wire anemometer
 31 (405i, Testo Co.) and a laser displacement sensor (HG-C1400, Panasonic.), respectively.

32 The amplitudes of the bluff body under different wind speeds obtained by experiments and
 33 numerical calculations are shown in Figure 5(b). It should be noted that $K = 8.816$ N/m and
 34 $C = 0.0077$ N·(m/s)⁻¹ ($\zeta = 0.018$) can be calculated from the free decaying oscillations. It
 35 can be seen that when the wind speed is larger than a critical wind speed, the bluff body
 36 begins to vibrate, and the amplitude increases along with the increase of the wind speed. The

1 experimental results are very close to the theoretical ones. Overall, the simulations from the
 2 theoretical model have a good agreement with the experimental measurements based on the
 3 employment of the aerodynamic coefficients. Thus, the aerodynamic coefficients $A_1 = 2.3$
 4 and $A_3 = -18$ are suitable in further numerical simulations of the present work.



5
 6 Figure 5 (a) The wind tunnel test setup and (b) the experimental data along with the theoretical curve.

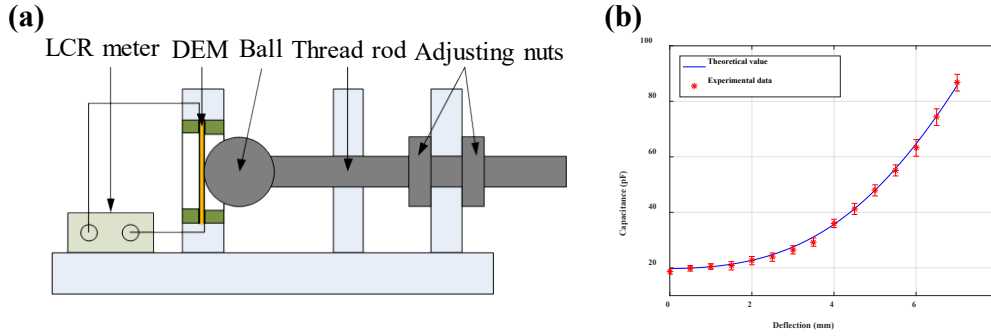
7 3.2 Identification of dielectric permittivity ε_r

8 Previous research has demonstrated that the relative permittivity ε_r is a function of
 9 pre-stretch ratio λ and temperature T [51], which can be expressed as:

$$10 \quad \varepsilon_r = a\lambda^2 + b/T + c \quad (16)$$

11 where $a = -0.053$, $b = 638$ and $c = 3.024$ are empirical constants. When $\lambda = 2$ and
 12 $T = 298.15$ K (25°C), it can be calculated through Eq. (16) that $\varepsilon_r = 4.9519$. In order to
 13 verify this result, a capacitance test was designed and carried out for the membrane in its
 14 static states, as shown in Figure 6.

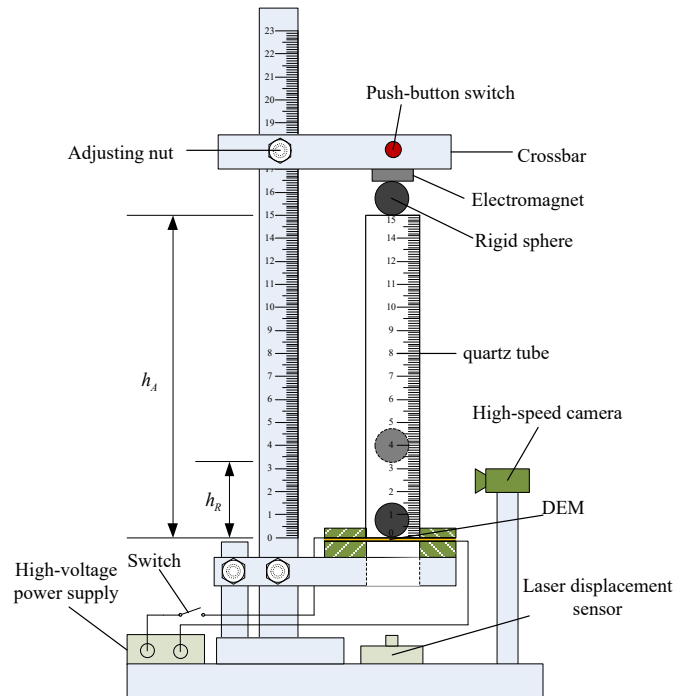
15 Figure 6(a) presents the experimental set-up, which consists of a fixed DEM with $\lambda = 2$
 16 ($R_0 = 6$ mm, $h_0 = 0.25$ mm), an LCR meter (4090A, Victor INC.), a ball ($r_b = 5$ mm)
 17 connecting to a threaded rod, and two adjusting nuts. Thus, the capacitances across the DEM
 18 can be measured using the LCR meter under different deflections, which are precisely
 19 controlled by the adjusting nuts. The experimental results are shown in Figure 6(b), along with
 20 the theoretical curve. It can be seen that the theoretical results agree with the experimental
 21 data well, thus verifying the theoretical approach in calculating the capacitance across the
 22 DEM under different deflections. It is noted that the error-bars in Figure 6(b) are obtained by
 23 recording the maximal and minimal capacitances of the DEMs at five different tests under
 24 each deflection, thus avoiding the experimental errors.



1
 2 Figure 6 (a) The experimental set-up for capacitance measurement and (b) the capacitance of the
 3 membrane at different deflections under pre-stretched ratio $\lambda = 2$ and temperature $T = 25^\circ\text{C}$.

4 3.3 Identification of COR r and largest deflection δ

5 The COR r and the largest deflection δ of a pre-stretched DEM under impacts are
 6 identified using the experimental set-up with a ball's free fall shown in Figure 7. The
 7 presented experimental set-up consists of a ball ($r_b = 5\text{ mm}$) with a mass of 3.5 g, a fixed
 8 pre-stretched DEM at the bottom of a quartz tube with a dimensional scale, a laser
 9 displacement sensor (HG-C1100, Panasonic) used to measure the membrane's deflection, an
 10 electromagnet connected to a crossbar whose height can be controlled precisely by the
 11 adjusting nut connected to a vertical ruler, a high-voltage power supply (71030P, BOHER)
 12 to produce input voltage for the DEM, and a camera to measure rebounding height of the ball.
 13 Here, h_A and h_R represent the dropping and rebounding heights of the ball, respectively. In
 14 this subsection, $V_{in} = 2000\text{ Volts}$ and $\lambda = 3$ were set in experiments.

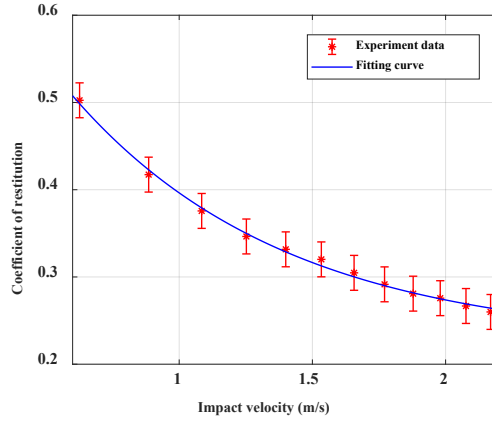


15
 16 Figure 7 Experimental set-up used to identify the COF and largest deflection of the DEM under the
 17 ball's impacts.

18 First, the CORs of the pre-stretched DEM under different impact velocities (decided by the

1 dropping height: $v = \sqrt{2gh_A}$) were calculated through $r = |v_{m+} / v_{m-}| = \sqrt{h_R / h_A}$ after
 2 measuring the dropping and rebounding heights of the ball. The experimental results are
 3 shown in Figure 8. It can be seen that as the impact velocity increases, the COR presents an
 4 exponentially decreasing curve. This can be explained that the higher the impact velocity the
 5 higher the internal energy losses thus decreasing the proportion between the rebound and
 6 impact velocities. The experimental data can be fitted using the following exponential
 7 equation, which will be used in further numerical calculations in this paper:

$$8 \quad r = 0.5989e^{-1.31v} + 0.2241 \quad (17)$$

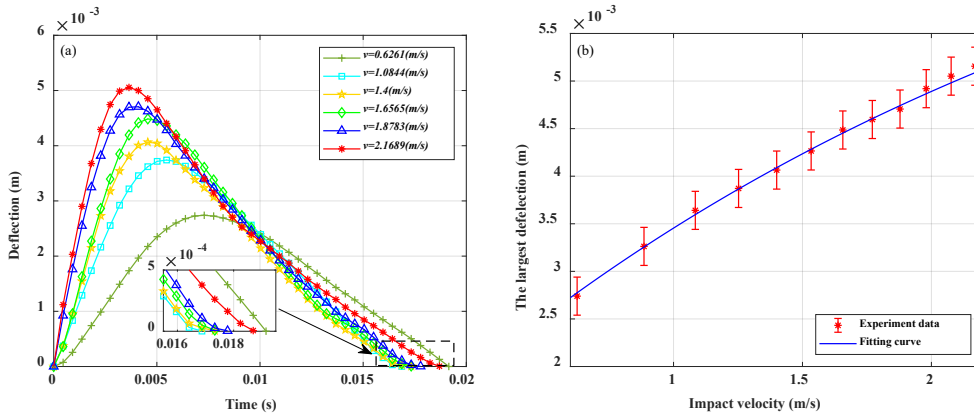


9

10 Figure 8 COR of the DEM against impact velocity ($V_{in} = 2000 \text{ V}$, $\lambda = 3$).

11 Next, the largest deflections of the DEM at impacts with different impact velocities were
 12 recorded through the laser displacement sensor, as shown in Figure 9(a), where the curves of
 13 deflections against time under different impact velocities are presented. It can be seen that the
 14 impact time (the time interval between two zero-crossing points of each curve), which is as
 15 small as around 0.17 s, is almost a constant under different impact velocities. Moreover, the
 16 largest deflection at each impact, which is the maximum value of each curve, presents an
 17 increasing trend as the velocity increases. This law is better presented in Figure 9(b), where
 18 one can see that the experimental data can be reasonably fitted with an exponential function,
 19 which will be used in further numerical calculations in this paper:

$$20 \quad \delta = -0.006903e^{-0.3498v} + 0.00832 \quad (18)$$



21

22 Figure 9 (a) Curves of deflections against time under different impact velocities and (b) largest
 23 deflection at each impact against the impact velocity.

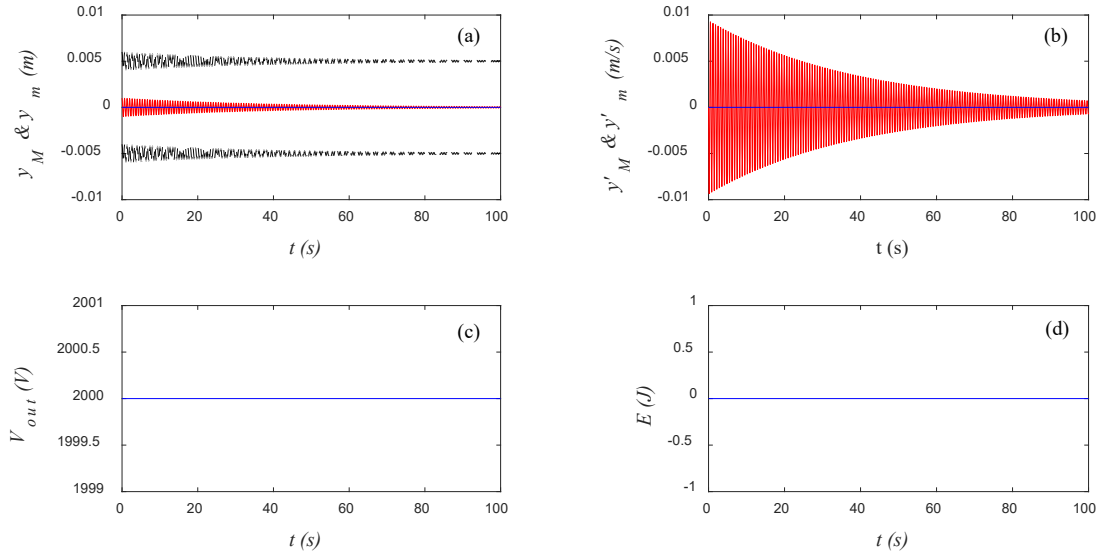
1 **4. Simulations**

2 It is difficult to obtain the system response analytically due to its highly nonlinear nature.
 3 Therefore, the fourth-order Runge-Kutta algorithm is adopted in this paper to solve the
 4 governing equations of the system. In this section, the dynamic behaviors of the bluff body
 5 and the VI DEG under different wind conditions are studied through numerical simulations,
 6 and the electrical outputs of the DEG system are presented as well. According to the analyses
 7 in the theoretical and experimental parts, the values of the parameters used in simulations are
 8 presented in Table 1 unless otherwise stated. Moreover, the initial position and velocity of the
 9 bluff body are set as $y_M(0)=1$ mm and $y'_M(0)=0$ in simulations. It should be noted that
 10 most parameters shown in Table 1 are the same as those in the experiments in Section 3, while
 11 the value of M is much larger than that in Figure 5(a) as the DEG is considered to be
 12 embedded into the bluff body. Thus, the critical wind speed for the bluff body to start
 13 vibrating will be increased apparently. Therefore, a larger range of the wind speed compared
 14 that in Figure 5(b) is considered in the numerical simulations.

15 Table 1 Values of parameters used in simulations

Parameter	Value	Parameter	Value	Parameter	Value
M	100 g	K	8.816 N/m	C	0.0077 N · s/m
L_C	200 mm	L	32 mm	H	118 mm
W	32 mm	T	25 °C	ρ	1.1846 kg/m ³
A_1	2.3	A_2	-18	β	11.67
l	32 mm	w	6 mm	r_b	5 mm
λ	3	m	3.5 g	R_0	6 mm
h_0	0.111 mm	ε_r	4.687	V_{in}	2000 V

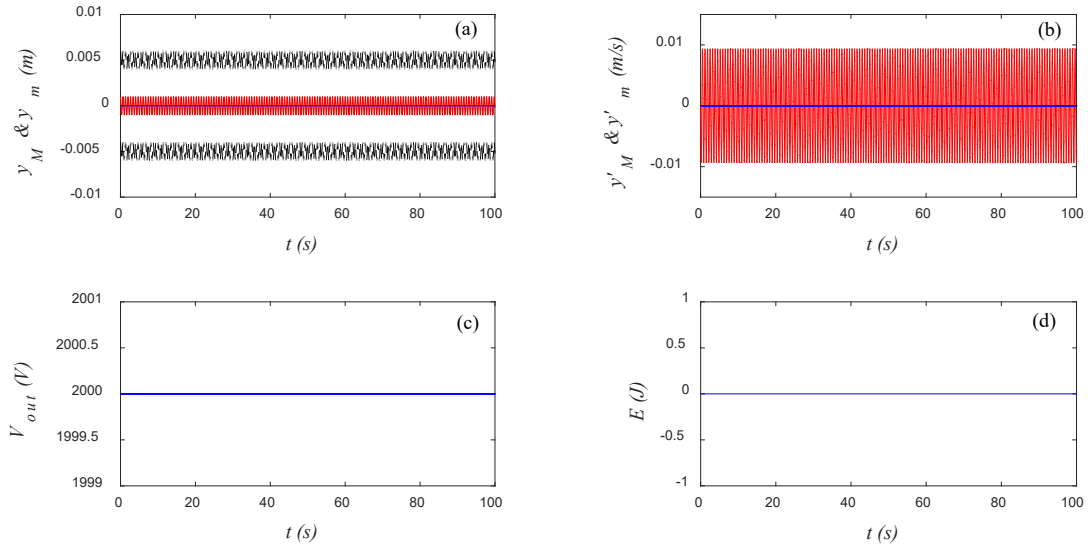
16
 17 First, a condition of small wind speed, such as $U = 0.5$ m/s, is considered and the system
 18 responses are shown in Figure 10. It can be seen from Figure 10(a, b) that as the wind speed is
 19 small, the bluff body recovers to its original position ($y_M = 0$) after a transient process. This
 20 indicates that the low-speed wind does not have enough energy to overcome the stiffness of
 21 the cantilever and excite the bluff body. Again, the simulated results agree with the
 22 experimental results shown in Figure 5(b) that the bluff body cannot vibrate when the wind
 23 speed is lower than the critical value. Thus, no impacts occur and no electrical energy can
 24 be harvested from the DEG, as shown in Figure 10(c, d) where the output voltage equals to
 25 the input voltage and the electrical energy gain is kept at 0 all the time.



1

2 Figure 10 System responses under $U = 0.5$ m/s. (a) The movement displacements of the bluff body
 3 and the ball are represented by the red solid line and the blue solid line, respectively; the black dashed
 4 lines indicate the positions of the left and right membranes; (b) the velocities of the bluff body and the
 5 ball are represented by the red solid line and the blue solid line, respectively; (c) the output voltage of
 6 the DEG against time; (d) the electrical energy gain of the DEG against time.

7 When the wind speed is increased to $U = 1.5$ m/s, the system responses are presented in
 8 Figure 11. It can be seen that the bluff body recovers slowly to its original position. That is,
 9 the displacement and velocity of the bluff body oscillate to 0 with much smaller rates than
 10 those in Figure 10, which means the wind has a greater effect on the bluff body but is not
 11 large enough to excite the bluff body yet. Again, no energy can be harvested under this
 12 condition.

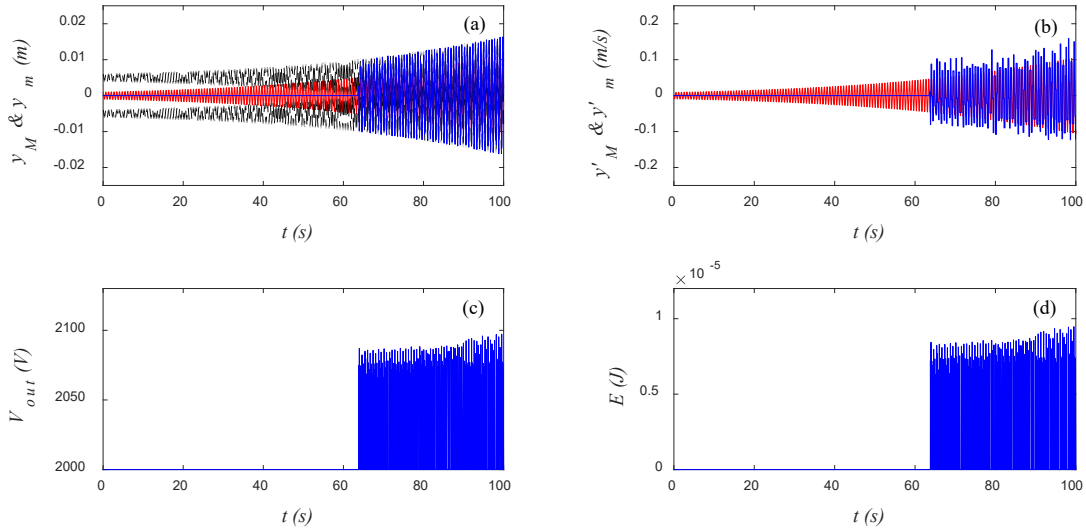


13

14 Figure 11 System responses under $U = 1.5$ m/s. (a) The movement displacements of the bluff body
 15 and the ball are represented by the red solid line and the blue solid line, respectively; the black dashed
 16 lines indicate the positions of the left and right membranes; (b) the velocities of the bluff body and the
 17 ball are represented by the red solid line and the blue solid line, respectively; (c) the output voltage of
 18 the DEG against time; (d) the electrical energy gain of the DEG against time.

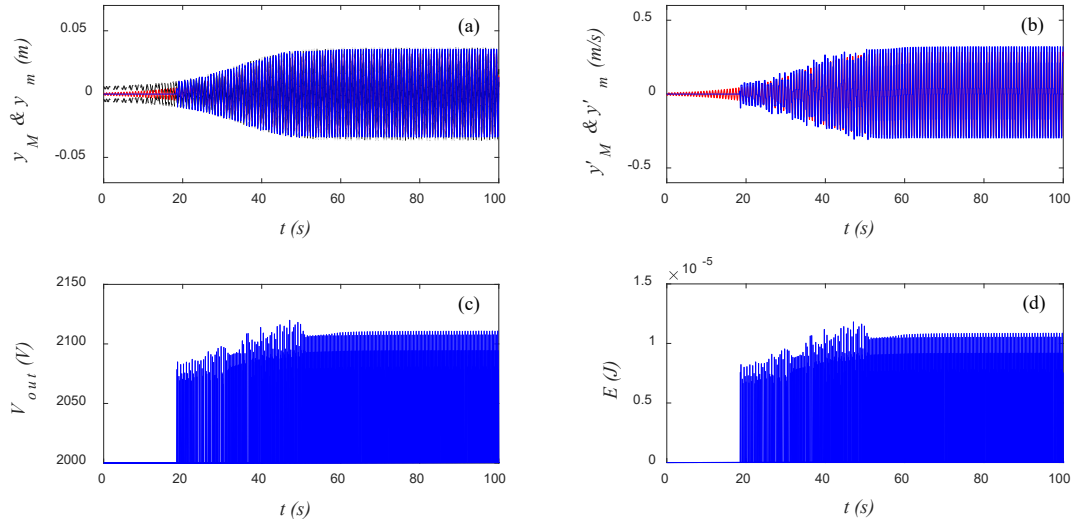
19 Situation changes when the wind speed is increased to $U = 2.5$ m/s, which is higher than

1 the critical wind speed. The system responses are shown in Figure 12. It can be seen from
 2 Figure 12(a, b) that the speed is high enough for the wind to overcome the stiffness of the
 3 cantilever. Hence, the bluff body is excited by the wind with its amplitudes of the
 4 displacement and velocity slowly increasing until the bluff body reaches an oscillatory steady
 5 state response. Moreover, as the vibrations amplitude of the bluff body increases to a certain
 6 value, the membranes start to impact the inner ball (the start time is around 64 s in this case).
 7 After that, the ball continues to impact both membranes leading to higher output voltage and
 8 electrical energy gained at each impact, as shown in Figure 12(c, d). It can be imagined that
 9 there must exist a lower critical value of the wind speed between 1.5 m/s and 2.5 m/s that
 10 enables the bluff body to oscillate continuously.

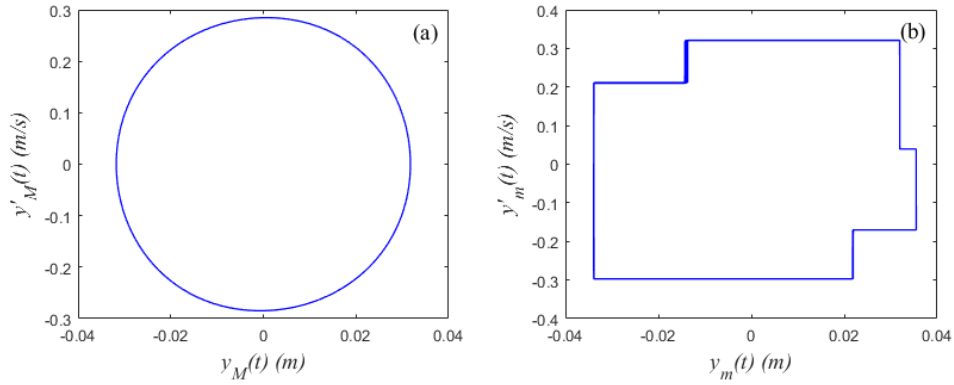


11
 12 Figure 12 System responses under $U = 2.5$ m/s. (a) The movement displacements of the bluff body
 13 and the ball are represented by the red solid line and the blue solid line, respectively; the black dashed
 14 lines indicate the positions of the left and right membranes; (b) the velocities of the bluff body and the
 15 ball are represented by the red solid line and the blue solid line, respectively; (c) the output voltage of
 16 the DEG against time; (d) the electrical energy gain of the DEG against time.

17 Continue to increase the wind speed to $U = 5$ m/s, the system responses are similar to
 18 those in Figure 12, as shown in Figure 13. It can be seen that the bluff body starts to vibrate
 19 under the wind until it reaches a steady state. This steady state can be also seen from Figure
 20 14, where the phase trajectories of the bluff body and the ball from 70 s to 100 s are plotted.
 21 The closed phase trajectories indicate that the bluff body and the ball are at steady states after
 22 a transient process with their displacements and velocities changing periodically. These steady
 23 states indicate the equilibrium between the wind and the system. Thus, impacts occur
 24 regularly and the electrical energy can be harvested continuously. The output power of the
 25 system at its steady state, for example, 70 s to 100 s, was calculated and equal to $P = 0.0795$
 26 mW.

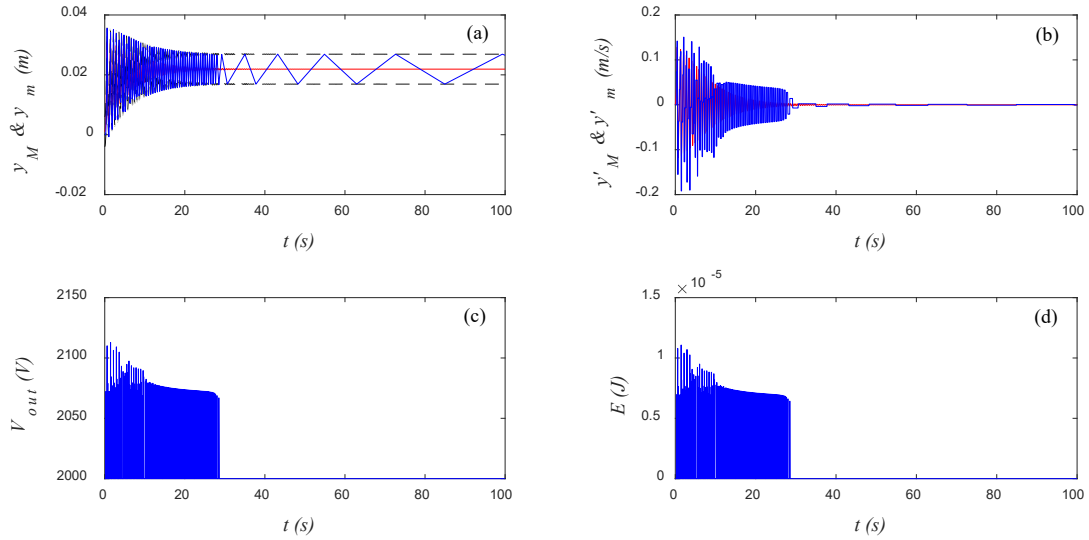


1
 2 Figure 13 System responses under $U = 5$ m/s. (a) The movement displacements of the bluff body
 3 and the ball are represented by the red solid line and the blue solid line, respectively; the black dashed
 4 lines indicate the positions of the left and right membranes; (b) the velocities of the bluff body and the
 5 ball are represented by the red solid line and the blue solid line, respectively; (c) the output voltage of
 6 the DEG against time; (d) the electrical energy gain of the DEG against time.



7
 8 Figure 14 The phase trajectories of (a) the bluff body and (b) the ball from 70 s to 100 s

9 However, the system response changes when the wind speed is being increased. The results
 10 under $U = 16$ m/s are shown in Figure 15, where one can see in Figure 15(a) that due to a
 11 high wind speed and after a transient process the bluff body stops at its static equilibrium state
 12 at one side of the cantilever's axis. This static equilibrium between the wind and the system,
 13 indicates that the bluff body is suffered from the strong wind and cannot vibrate anymore. The
 14 ball still impacts the membranes a couple of times and stops finally due to the energy losses at
 15 impacts. Therefore, electrical energy can be gained at the beginning of this process but no
 16 more energy can be gained later. The results indicate that the proposed system with the given
 17 parameters cannot work effectively under a wind speed higher than an upper critical wind
 18 speed. To gain energy from such a high wind speed one has to adjust the system parameters
 19 appropriately.



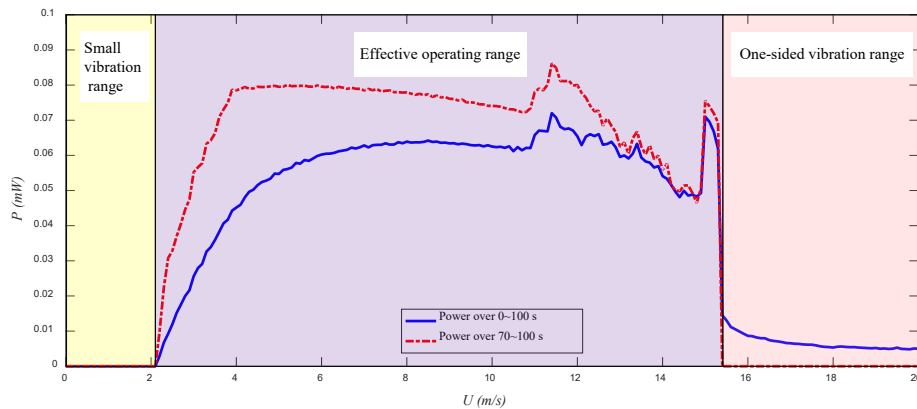
1
2 Figure 15 System responses under $U = 16$ m/s. (a) The movement displacements of the bluff body
3 and the ball are represented by the red solid line and the blue solid line, respectively; the black dashed
4 lines indicate the positions of the left and right membranes; (b) the velocities of the bluff body and the
5 ball are represented by the red solid line and the blue solid line, respectively; (c) the output voltage of the
6 DEG against time; (d) the electrical energy gain of the DEG against time.

7 5. Discussion

8 It can be seen from Section 4 that the EH performance of the proposed system is
9 significantly affected by the wind speed. To better reveal this influence, the EH performance
10 under different wind speeds are studied in this section. Moreover, the influence of the system
11 parameters such as the stiffness and the distance between two DEMs are analyzed as well in
12 this section.

13 5.1 VEH performance under different wind speed

14 It can be seen from Section 4 that the proposed system has different dynamic behaviors and
15 electrical outputs under different wind speeds. In order to further present the system energy
16 harvesting performance, which we concern most for the potential application of the system,
17 the system averaged output power against wind speed (0~20 m/s) is plotted in Figure 16. It
18 should be noted that the blue solid line presents the averaged output power over 0~100 s, and
19 the red dashed line presents that over 70~100 s, where the stable operating condition of the
20 system was observed.



21
22 Figure 16 System average output power against wind speed

1 It can be seen from Figure 16 that as the wind speed increases from 0 m/s to as large as 20
2 m/s, the power curves can be divided into three regions. In the first region, which represents
3 the small vibrations range of the wind speed ($0 \leq U \leq 2.1$ m/s), the wind energy is weak, so
4 the bluff body vibrates from its initial position to an approximately steady state due to the
5 damping of the cantilever. Within this range of wind speeds no impacts occur between the ball
6 and the membranes and no electrical energy can be harvested, as shown in Figure 10 and
7 Figure 11. The second region, which is termed as an effective operating range of the wind
8 speed ($2.1 \leq U \leq 15.4$ m/s), indicates the range of the wind speed among which the wind
9 energy is strong enough to force the bluff body to vibrate accordingly, thus enabling the ball
10 to impact both membranes producing electrical energy, as shown in Figure 12 and Figure 13.
11 Inside this range, the averaged output power over 70~100 s is larger than that over 0~100 s as
12 the transition process with no impacts occurring is ignored for the former curve. It can be also
13 seen that under most wind speeds within this range the averaged output powers over 70~100 s
14 are larger than 0.07 mW (the largest one is around 0.09 mW), indicating that the system has a
15 continuous operating range with relatively high output power. The right region is called a
16 one-sided vibration domain, which means the wind speed among this range ($U \geq 15.4$ m/s) is
17 so strong that the bluff body is restricted at one of its two stable equilibrium points and cannot
18 transit to another equilibrium state. Therefore, after the transition process the bluff body stops
19 vibrating and only several sporadic impacts occur, thus producing almost no electrical energy.
20 It should be noted that the average output power over 0~100 s is larger than those over
21 70~100 s because the impacts occurred in the transition are taken into account.

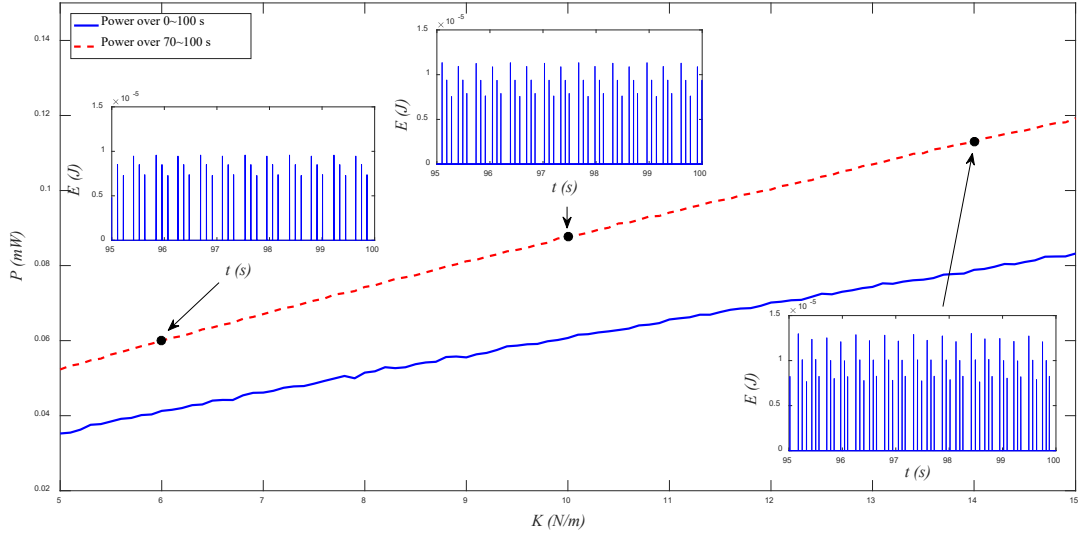
22 It is notable that the effective working region of the wind speed from 2.1 m/s to 15.4 m/s
23 can cover the common velocities in natural environments such as the light breeze (1.6-3.3 m/s)
24 gentle breeze (3.4~5.4 m/s), moderate breeze (5.5~7.9 m/s), fresh breeze (8~10.7 m/s), strong
25 breeze (10.8~13.8 m/s) and moderate gale (13.9~17.1 m/s). Therefore, the proposed system
26 shows one of its advantages that it is suitable to operate in a common wind speed conditions
27 with a relative high output power.

28 **5.2 Influence of the stiffness on the system VEH performance**

29 Besides the wind speed, the system parameters also have an influence on the system VEH
30 performance. Among the parameters presented in Table 1, some of them are intercoupling.
31 For example, the value L_b affects the values of C and K ; the value of ρ is decided by
32 T ; the value of ε_r is decided by T and λ ; the values of m , r_b , λ , R_0 , h_0 and V_{in}
33 affect the value of r and δ in each impact. Therefore, the influences of these parameters
34 on the system VEH performance are not easy to analyze. In this subsection, we first consider
35 the influence of the stiffness K on the system EH performance.

36 The value of K can be easily adjusted by changing the material and length of the
37 cantilever, thus making it a variable parameter that can affect the system VEH performance.
38 Figure 17 presents the average output powers of the system against the stiffness under $U = 5$
39 m/s. It can be seen that both the power over 0~100 s and over 70~100 s show an increasing
40 trend as the value of K increases. In order to better illustrate the influence of K , three
41 subplots are presented to show the energy gain between 95 s and 100 s (indicating the stable
42 operating condition) under $K = 6$, $K = 10$ and $K = 14$. It can be seen that as the value of
43 K increases, more impacts occur during a certain time interval because a high stiffness

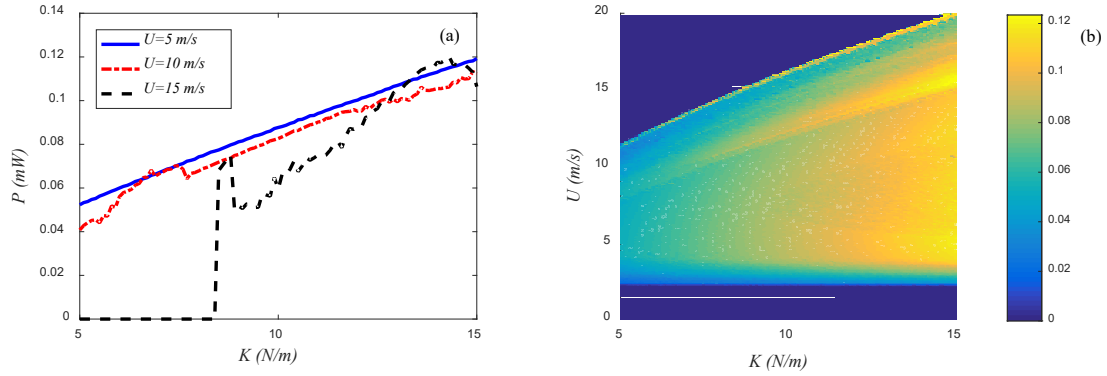
1 makes the bluff body change its velocity quicker due to a higher natural frequency of the
 2 system. Moreover, a stronger stiffness makes the bluff body move faster generally, thus
 3 producing higher averaged energy gain. Therefore, more electrical energy can be harvested
 4 during a certain time interval and a higher average output power can be produced under a
 5 larger stiffness. This provides a possible solution to improve the VEH performance of the
 6 proposed system by increasing the stiffness reasonably.



7
 8

Figure 17 System output power against the stiffness under $U = 5$ m/s

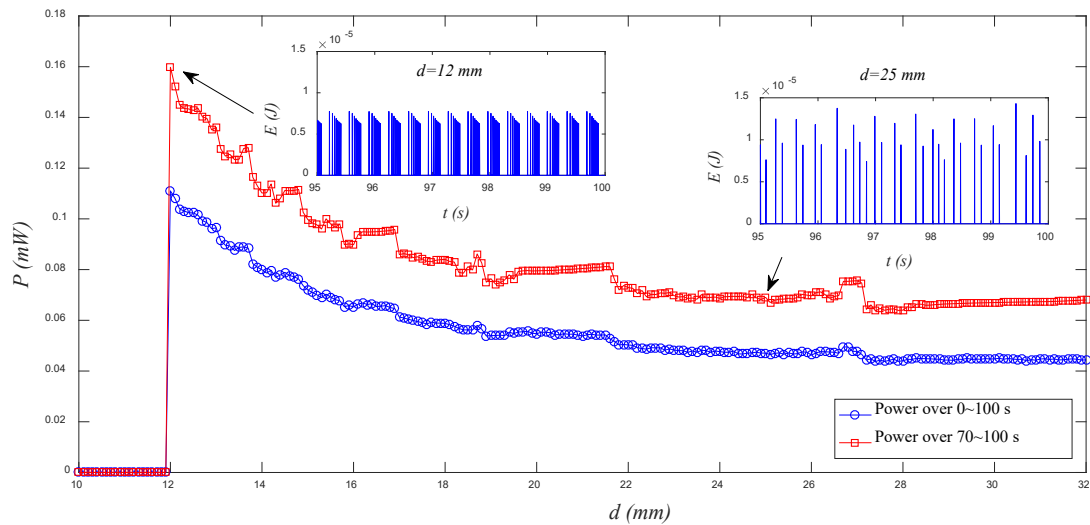
9 Similar curves are presented in Figure 18(a) under different wind speeds ($U = 5, 10, 15$
 10 m/s). It can be seen that all curves show a general increasing trend as the value of K
 11 increases. It should be noted that when $U = 15$ m/s, as the value of K increases, the
 12 curve starts from a zero-line, indicating that the wind speed is among the one-sided vibrations
 13 range under such a small stiffness. In order to better reveal this phenomenon, the averaged
 14 output power of the system under different sets of K and U is plotted in Figure 18(b). It
 15 can be seen that on one side, under a given K , the wind speeds can be divided into a small
 16 vibrations range, effective operating region and one-sided vibrations domain, as shown in
 17 Figure 16. Moreover, the lower critical value between is kept almost as a constant as the value
 18 of K changes, indicating that the proposed system starts to harvest energy from a constant
 19 minimal wind speed. While the upper critical value between the effective operating region
 20 and the one-sided vibrations domain increases as the value of K increases, indicating that a
 21 larger K value can expand the effective operating range to a higher wind speeds. On the
 22 other hand, under a given U the output power increases as the value of K increases
 23 among the effective operating range, which corresponds to the rules shown in Figure 17 and
 24 Figure 18(a).



1
2 Figure 18 System average output power over 70~100 s (a) against stiffness under different wind
3 speeds and (b) under different sets of stiffness and wind speed.

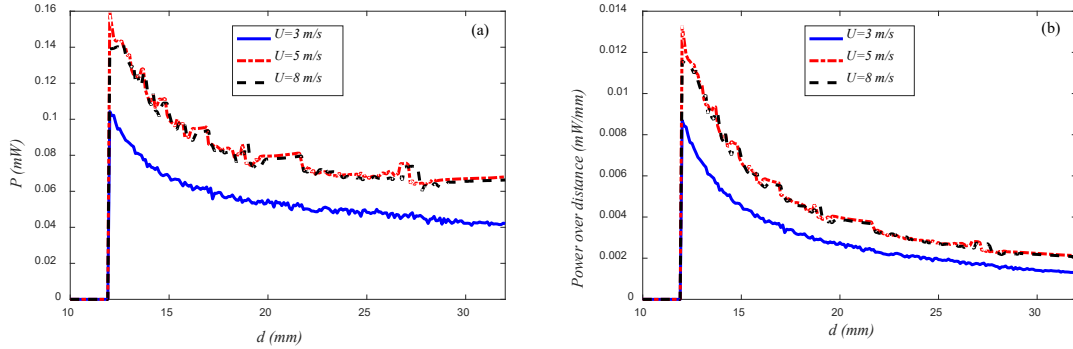
4 5.3 Influence of the distance between two DEMs on the system VEH performance

5 The influence of the distance between two DEMs on the system VEH performance is
6 analyzed in this subsection. This distance, which is defined as $d = l - 2w$ in this paper,
7 should be larger than the ball's diameter and smaller than the bluff body's width
8 ($2r_b < d < W$). Thus, the average output power of the proposed system under $U = 5$ m/s,
9 with d varying from 10 mm ($2r_b$) to 32 mm (W) and other parameters kept as those in
10 Table 1, is presented in Figure 19. It can be seen that the curve starts from a zero-line, which
11 indicates that the ball moves almost following the DEMs due to the small distance, thus
12 producing no impacts and electrical energy. The curve then grows sharply to its largest value.
13 The energy gain between 95 s and 100 s is presented under $d = 12$ mm. It can be seen that
14 under the optimal distance between two DEMs the ball impact the DEMs regularly and a
15 relatively high output power is realized. Next, the curve drops gradually to some almost
16 constant value. The energy gain between 95 s and 100 s under $d = 25$ mm tells that although
17 the impact strength may be larger when d is larger, less impacts number resulting from the
18 larger d makes the system produce lower output power than that at the optimal distance
19 condition. It can be concluded that there exists an optimal distance between two DEMs that
20 makes the system produce the largest output power.



21
22 Figure 19 System output power against the distance between two DEMs under $U = 5$ m/s.

1 Similar curves are presented in Figure 20(a) under different wind speeds ($U = 3, 5, 8$
 2 m/s). It can be seen that all curves have the similar trend as described previously for Figure 19.
 3 Moreover, the power over distances (P/d) are presented in Figure 20(b) for different
 4 distances d . The dimensional curves are better to show the VEH performance of the
 5 proposed system under different distances between the DEMs. It can be seen that the curves
 6 start from a zero-line, and drop slightly after they grow sharply to their largest values. The
 7 results shown in Figure 20(a, b) tells that d can be selected as an optimization parameter in
 8 the design of the proposed system.



9
 10 Figure 20 (a) Average output power and (b) average output power over distance against the distance
 11 between two DEMs.

12 6. Conclusion

13 A novel wind energy harvester, which consists of a galloping-based cuboid bluff body, a
 14 cantilever beam and a VI DEG embedded horizontally in the bluff body, is proposed in this
 15 paper. The dynamic behavior of the bluff body under wind are analyzed. With the dynamic
 16 output of the bluff body as the input of the DEG, the vibrations resulting from the wind
 17 energy can be harvested by the VI DEG, and the detailed energy harvesting process is studied.
 18 Next, some key parameters in the theoretical analysis are identified through experiments. A
 19 wind tunnel experiment is conducted to verify the empirical constants in the equation to
 20 calculate the galloping force; a capacitance measurement was designed to identify the relative
 21 permittivity of the DEM; an impact experiment was conducted to study the relations of the
 22 coefficient of restitution and the largest deflection of the DEM against the impact velocity.
 23 Thus, precise numerical results have been obtained. Further, the dynamic and electrical
 24 outputs of the system under different wind speeds were studied through numerical simulations.
 25 It was found that wind energy could be harvested by the proposed system when the wind
 26 speed was appropriate. The influences of the wind and some system parameters including the
 27 stiffness and distance between DEMs on the system EH performance were discussed. It was
 28 found that under the given parameters, the proposed system can operate effectively within the
 29 relatively wide wind speed range from 2.1 m/s to 15.4 m/s, which involves the common wind
 30 speed range in practical environments, with a relatively high output power of 0.09 mW.
 31 Moreover, by increasing the stiffness of the system and adjusting the distance between the
 32 DEMs appropriately, the output power can be further enhanced up to 0.16 mW. The research
 33 results have shown the advantage of the proposed system in wind energy harvesting and
 34 provide useful guidelines for the design and improvement of the system.

1 Acknowledgment

2 This work is supported by the National Natural Science Foundation of China (No: 51606171),
3 China Postdoctoral Science Foundation (No. 2019M652565), Natural Science Foundation of
4 Jiangxi Province (CN) (Grant No. 20161BAB216111), Natural Science Foundation of
5 Shenzhen University (Grant No. 2019036), and Key Laboratory of Lightweight and High
6 Strength Structural Materials of Jiangxi Province (Grant No. 20171BCD40003).

7 Reference

- 8 [1] C. F. Wei, X. J. Jing. A comprehensive review on vibration energy harvesting: Modelling and
9 realization. *Renewable & Sustainable Energy Reviews*, 2017, **74**: 1-18.
- 10 [2] J. Song, G. Hu, K. Tse, S. Li, K. Kwok. Performance of a circular cylinder piezoelectric wind
11 energy harvester fitted with a splitter plate. *Applied Physics Letters*, 2017, **111**(22): 223903.
- 12 [3] G. Hu, K.-T. Tse, K. C. Kwok, J. Song, Y. Lyu. Aerodynamic modification to a circular cylinder
13 to enhance the piezoelectric wind energy harvesting. *Applied Physics Letters*, 2016, **109**(19):
14 193902.
- 15 [4] X. He, X. Yang, S. Jiang. Enhancement of wind energy harvesting by interaction between
16 vortex-induced vibration and galloping. *Applied Physics Letters*, 2018, **112**(3): 033901.
- 17 [5] M. Cheng, Y. Zhu. The state of the art of wind energy conversion systems and technologies: A
18 review. *Energy Conversion and Management*, 2014, **88**: 332-347.
- 19 [6] F. K. Shaikh, S. Zeadally. Energy harvesting in wireless sensor networks: A comprehensive
20 review. *Renewable & Sustainable Energy Reviews*, 2016, **55**: 1041-1054.
- 21 [7] S. Wu, P. C. K. Luk, C. Li, X. Zhao, Z. Jiao, Y. Shang. An electromagnetic wearable 3-dof
22 resonance human body motion energy harvester using ferrofluid as a lubricant. *Applied Energy*,
23 2017, **197**: 364-374.
- 24 [8] H. Xiong, L. Wang. Piezoelectric energy harvester for public roadway: On-site installation and
25 evaluation. *Applied Energy*, 2016, **174**: 101-107.
- 26 [9] J. W. Matiko, N. J. Grabham, S. P. Beeby, M. J. Tudor. Review of the application of energy
27 harvesting in buildings. *Measurement Science and Technology*, 2014, **25**(1).
- 28 [10] Z. Chen, B. Guo, Y. Yang, C. Cheng. Metamaterials-based enhanced energy harvesting: A
29 review. *Physica B-Condensed Matter*, 2014, **438**: 1-8.
- 30 [11] E. Varadha, S. Rajakumar. Performance improvement of piezoelectric materials in energy
31 harvesting in recent days - a review. *Journal of Vibroengineering*, 2018, **20**(7): 2632-2650.
- 32 [12] H. Liu, J. Zhong, C. Lee, S.-W. Lee, L. Lin. A comprehensive review on piezoelectric energy
33 harvesting technology: Materials, mechanisms, and applications. *Applied Physics Reviews*, 2018,
34 **5**(4).
- 35 [13] S. Zhou, L. Zuo. Nonlinear dynamic analysis of asymmetric tristable energy harvesters for
36 enhanced energy harvesting. *Communications in Nonlinear Science and Numerical Simulation*,
37 2018, **61**: 271-284.
- 38 [14] D. M. Huang, S. X. Zhou, G. Litak. Theoretical analysis of multi-stable energy harvesters with
39 high-order stiffness terms. *Communications in Nonlinear Science and Numerical Simulation*,
40 2019, **69**: 270-286.
- 41 [15] Y. Gao, Y. Leng, A. Javey, D. Tan, J. Liu, S. Fan, Z. Lai. Theoretical and applied research on
42 bistable dual-piezoelectric-cantilever vibration energy harvesting toward realistic ambience.
43 *Smart Materials and Structures*, 2016, **25**(11): 115032.
- 44 [16] I. Izadgoshasb, Y. Y. Lim, L. Tang, R. V. Padilla, Z. S. Tang, M. Sedighi. Improving efficiency
45 of piezoelectric based energy harvesting from human motions using double pendulum system.
46 *Energy Conversion and Management*, 2019, **184**: 559-570.
- 47 [17] K. Fan, Y. Zhang, H. Liu, M. Cai, Q. Tan. A nonlinear two-degree-of-freedom electromagnetic
48 energy harvester for ultra-low frequency vibrations and human body motions. *Renewable
49 Energy*, 2019, **138**: 292-302.
- 50 [18] Y. Zhang, J. Cao, H. Zhu, Y. Lei. Design, modeling and experimental verification of circular
51 halbach electromagnetic energy harvesting from bearing motion. *Energy Conversion and
52 Management*, 2019, **180**: 811-821.
- 53 [19] Y. Zhang, T. Wang, A. Zhang, Z. Peng, D. Luo, R. Chen, F. Wang. Electrostatic energy
54 harvesting device with dual resonant structure for wideband random vibration sources at low
55 frequency. *Review of Scientific Instruments*, 2016, **87**(12).
- 56 [20] B. Chen, Y. Yang, Z. L. Wang. Scavenging wind energy by triboelectric nanogenerators.

- 1 *Advanced Energy Materials*, 2018, **8**(10).
- 2 [21] S. Zhou, J. Wang. Dual serial vortex-induced energy harvesting system for enhanced energy
3 harvesting. *AIP Advances*, 2018, **8**(7): 075221.
- 4 [22] J. Wang, L. Tang, L. Zhao, Z. Zhang. Efficiency investigation on energy harvesting from
5 airflows in hvac system based on galloping of isosceles triangle sectioned bluff bodies. *Energy*,
6 2019, **172**: 1066-1078.
- 7 [23] J. Wang, S. Zhou, Z. Zhang, D. Yurchenko. High-performance piezoelectric wind energy
8 harvester with y-shaped attachments. *Energy Conversion and Management*, 2019, **181**: 645-652.
- 9 [24] A. I. Aquino, J. K. Calautit, B. R. Hughes. Evaluation of the integration of the wind-induced
10 flutter energy harvester (wifeh) into the built environment: Experimental and numerical analysis.
11 *Applied Energy*, 2017, **207**: 61-77.
- 12 [25] J. Wang, L. Geng, M. Zhang, G. Zhao, M. Zhang, Z. Zhang, Y. Li. Broadening band of wind
13 speed for aeroelastic energy scavenging of a cylinder through buffeting in the wakes of a
14 squared prism. *Shock and Vibration*, 2018, **2018**.
- 15 [26] J. S. Huang, S. Shian, Z. G. Suo, D. R. Clarke. Maximizing the energy density of dielectric
16 elastomer generators using equi-biaxial loading. *Advanced Functional Materials*, 2013, **23**(40):
17 5056-5061.
- 18 [27] T. G. McKay, B. M. O'Brien, E. P. Calius, I. A. Anderson. Soft generators using dielectric
19 elastomers. *Applied Physics Letters*, 2011, **98**(14).
- 20 [28] S. Y. Yang, X. H. Zhao, P. Sharma. Avoiding the pull-in instability of a dielectric elastomer film
21 and the potential for increased actuation and energy harvesting. *Soft Matter*, 2017, **13**(26):
22 4552-4558.
- 23 [29] R. Pelrine, R. Kornbluh, J. Eckerle, P. Jeuck, S. J. Oh, Q. B. Pei, S. Stanford. *Dielectric*
24 *elastomers: Generator mode fundamentals and applications*. in *Smart Structures and Materials*
25 *2001: Electroactive Polymer Actuators and Devices*. 2001.
- 26 [30] P. Fan, L. Zhu, H. Chen, B. Luo. Energy harvesting from a de-based soft pendulum. *Smart*
27 *Materials and Structures*, 2018, **27**(11): 115023.
- 28 [31] C. Jean-Mistral, T. V. Cong, A. Sylvestre. Advances for dielectric elastomer generators:
29 Replacement of high voltage supply by electret. *Applied Physics Letters*, 2012, **101**(16):
30 162901.
- 31 [32] S. J. A. Koh, X. H. Zhao, Z. G. Suo. Maximal energy that can be converted by a dielectric
32 elastomer generator. *Applied Physics Letters*, 2009, **94**(26).
- 33 [33] R. Panigrahi, S. K. Mishra. An electrical model of a dielectric elastomer generator. *Ieee*
34 *Transactions on Power Electronics*, 2018, **33**(4): 2792-2797.
- 35 [34] T. G. McKay, S. Rosset, I. A. Anderson, H. Shea. Dielectric elastomer generators that stack up.
36 *Smart Materials and Structures*, 2015, **24**(1).
- 37 [35] Z. Suo, X. Zhao, W. H. Greene. A nonlinear field theory of deformable dielectrics. *Journal of*
38 *the Mechanics and Physics of Solids*, 2008, **56**(2): 467-486.
- 39 [36] J.-S. Plante, S. Dubowsky. Large-scale failure modes of dielectric elastomer actuators.
40 *International Journal of Solids and Structures*. 2006, **43**(25-26): 7727-7751.
- 41 [37] A. Schmidt, P. Rothmund, E. Mazza. Multiaxial deformation and failure of acrylic elastomer
42 membranes. *Sensors and Actuators A: Physical*, 2012, **174**: 133-138.
- 43 [38] S. J. A. Koh, C. Keplinger, T. F. Li, S. Bauer, Z. G. Suo. Dielectric elastomer generators: How
44 much energy can be converted? *Ieee-Asme Transactions on Mechatronics*, 2011, **16**(1): 33-41.
- 45 [39] A. Tröls, A. Kogler, R. Baumgartner, R. Kaltseis, C. Keplinger, R. Schwödiauer, I. Graz, S.
46 Bauer. Stretch dependence of the electrical breakdown strength and dielectric constant of
47 dielectric elastomers. *Smart Materials and Structures*, 2013, **22**(10): 104012.
- 48 [40] Y. Zhu, H. Wang, D. Zhao, J. Zhao. Energy conversion analysis and performance research on a
49 cone-type dielectric electroactive polymer generator. *Smart Materials and Structures*, 2011,
50 **20**(11): 115022.
- 51 [41] S. Shian, J. S. Huang, S. J. Zhu, D. R. Clarke. Optimizing the electrical energy conversion cycle
52 of dielectric elastomer generators. *Advanced Materials*, 2014, **26**(38): 6617-6621.
- 53 [42] G. Moretti, G. P. R. Papini, M. Righi, D. Forehand, D. Ingram, R. Vertechy, M. Fontana.
54 Resonant wave energy harvester based on dielectric elastomer generator. *Smart Materials and*
55 *Structures*, 2018, **27**(3): 035015.
- 56 [43] S. Chiba, M. Waki, T. Wada, Y. Hirakawa, K. Masuda, T. Ikoma. Consistent ocean wave energy
57 harvesting using electroactive polymer (dielectric elastomer) artificial muscle generators.
58 *Applied Energy*, 2013, **104**: 497-502.
- 59 [44] T. Vu-Cong, C. Jean-Mistral, A. Sylvestre. Electrets substituting external bias voltage in
60 dielectric elastomer generators: Application to human motion. *Smart Materials and Structures*,

1 2013, **22**(2): 025012.

2 [45] Z. H. Lai, G. Thomson, D. Yurchenko, D. V. Val, E. Rodgers. On energy harvesting from a
3 vibro-impact oscillator with dielectric membranes. *Mechanical Systems and Signal Processing*,
4 2018, **107**: 105-121.

5 [46] D. Yurchenko, D. V. Val, Z. H. Lai, G. Gu, G. Thomson. Energy harvesting from a de-based
6 dynamic vibro-impact system. *Smart Materials and Structures*, 2017, **26**(10): 105001.

7 [47] D. Yurchenko, Z. H. Lai, G. Thomson, D. V. Val, R. V. Bobryk. Parametric study of a novel
8 vibro-impact energy harvesting system with dielectric elastomer. *Applied Energy*, 2017, **208**:
9 456-470.

10 [48] L. Zhao, Y. Yang. Enhanced aeroelastic energy harvesting with a beam stiffener. *Smart*
11 *Materials & Structures*, 2015, **24**(3).

12 [49] L. Tang, L. Zhao, Y. Yang, E. Lefeuve. Equivalent circuit representation and analysis of
13 galloping-based wind energy harvesting. *IEEE/ASME Transactions on Mechatronics*, 2014,
14 **20**(2): 834-844.

15 [50] G. Thomson, Z. H. Lai, D. V. Val, D. Yurchenko. Advantages of nonlinear energy harvesting
16 with dielectric elastomers. *Journal of Sound and Vibration*, 2019, **442**: 167-182.

17 [51] J. Sheng, H. Chen, B. Li, Y. Wang. Influence of the temperature and deformation-dependent
18 dielectric constant on the stability of dielectric elastomers. *Journal of Applied Polymer Science*,
19 2013, **128**(4): 2402-2407.

20

21